Polar Meteorol. Glaciol., **14**, 16–26, 2000

A laser tomograph technique for ice core stratigraphy analysis

Morimasa Takata[1] and Yoshiyuki Fujii[2]

[1] *The Graduate University for Advanced Studies, Kaga 1-chome, Itabashi-ku, Tokyo 173-8515*
[2] *National Institute of Polar Research, Kaga 1-chome, Itabashi-ku, Tokyo 173-8515*

Abstract: We have developed a laser tomograph system to analyze the detailed stratigraphic structure of ice core samples. We use a He-Ne laser as the light source and a CCD camera as a detector of a scattered image of air bubbles in ice. An image of air bubble distribution in the ice sample is obtained by image analysis of the scattered images. Two different algorithms are employed in the image analysis in order to improve the laser tomograph images. A profile of pore ratios obtained by using optimum conditions and algorithms for the analysis shows a good correlation of 0.80 with the actual pore ratio profile.

1. Introduction

A matrix of newly deposited snow on an inland ice sheet has a complex texture due to wind packing, sublimation, condensation and radiation melting at the surface. The snow then transforms into firn, changing its texture with depth hoar formation and densification near the surface to a shallow depth. A layered structure is formed to reflect meteorological conditions at the time of snow deposition and transformation. Density of firn increases with depth and reaches about 830 kgm^{-3} where firn becomes ice. Below this depth, stratigraphic features are preserved in ice as a difference in air bubble distribution.

Some methods have been developed to detect the stratigraphic features of the snow, firn and/or ice (Kimura, 1983; Kawamura, 1990; Azuma *et al.*, 1994; Hori *et al.*, 1999), but they require a large measuring system or the ability to analyze a structure with low spatial resolution. Gerland *et al.* (1999) measured a detailed density profile using a γ-ray technique, but it can only provide density information. Some laser techniques have been applied to ice core analysis. Ram *et al.* (1995) developed a laser scattering technique to analyze number of dust particles in deeper parts of ice cores where air bubbles change to air-hydrates. Fujii (1997) used a laser tomograph technique for stratigraphy analysis of air-hydrates in ice cores. In this paper, we describe a newly improved technique using a laser tomograph. This technique makes high resolution and speedy stratigraphic analysis possible by measuring the detailed air bubble distribution.

2. Methods

Figure 1 shows a schematic drawing of the measuring system. Details of the system components are listed in Table 1. The ice sample is irradiated by a He-Ne laser beam of 633 nm wavelength, 0.48 mm in diameter. The scattering image of an ice sample by the laser irradiation is detected by a CCD camera. The laser head and the CCD camera are installed on the same moving stage, and are moved simultaneously along the sample at a constant speed of about 5 mm s^{-1}. While the stage is in motion, scattering images are recorded continuously onto a digital video recorder.

When an ice sample is irradiated by a laser beam, the ice glitters around the incident point of the laser beam and at several points in the ice by scattering. The scattering occurs at surfaces of air bubbles, grain boundaries and dust particles due to the difference in the index of refraction. For bubbly ice samples, scattering from surfaces of air bubbles is dominant because the scattering from fine dust particles and grain boundaries is weak. Therefore, we can detect stratigraphic features of ice samples by analyzing the scattering images.

The images recorded by a digital video recorder are stored in a personal computer

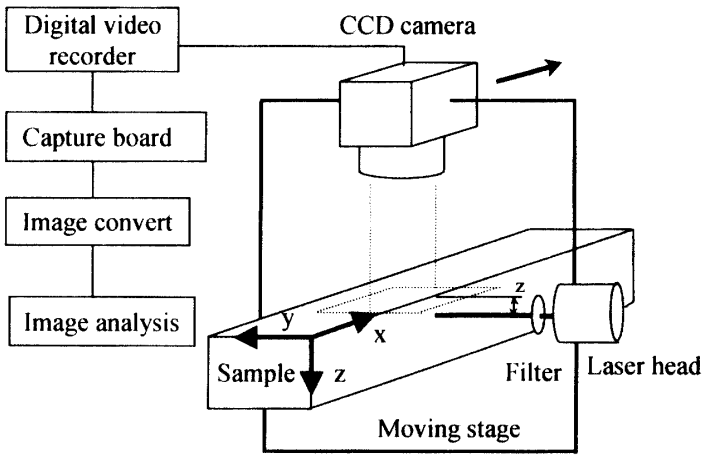

Fig. 1. Schematic drawing of the laser tomograph measurement system.

Table 1. Details of system components of the laser tomograph measurement and analysis software.

System component	Productive company	Model #
Laser	Uniphase	1107 P
Fillter	Sigumakoki	AMD-20C-50
CCD camera	Toshiba	IK-C40
Camera lense	Toshiba	JK-L12P
Digital video	Sony	DSR-30
Capture board	Adaptec	AHA8945
Image analysis software	Research Systems Inc.	IDL
Image convert software*[1]	K. Iwamoto	Video Maid
Image convert software*[2]	K. Nagahashi	Art Streamer

*[1] Conversion of AVI to Bitmap.

*[2] Conversion of Bitmap to JPEG of glay-scale.

as a movie file, AVI format with Dvsoft(TM) compression. The movie files are converted to image files, full color BMP format, for image analysis. The total size of all the images combined, however, becomes large since the size of each full color image is 1.3 Mbytes, and the movie file is composed of 30 images per second, *i.e.* images are taken at 0.17 mm intervals. However, since the actual image analysis requires only gray-scale, 256 level, images, all the images obtained in the measurement are converted to gray-scale images, and the BMP format is also converted to JPEG format. This reduces the file size to a manageable size.

Measurements are carried out under the following conditions: the stage moves at a speed of about 5 mm s^{-1} which means that it is possible to record the scattering images along a 50 cm long ice core within 100 seconds. The laser irradiation point is $z=1$ mm (see Fig. 1), which is suitable to detect scattering from air bubbles around the laser beam axis. The intensity of the laser beam is reduced to 50% using a filter. In this study, a sample 9 cm in length from iceberg ice is used; the sample contains air bubbles on the order of mm. Observation and laser incidence surfaces of the ice sample are made flat with a microtome. These conditions are suitable for image analysis of the scattering from air bubbles.

In order to evaluate the result of laser tomograph measurements, we need to know the distribution of air bubbles in the ice sample. Nishida and Narita (1996) determined crystal shapes three-dimensionally by integrating a series of two-dimensional images. We apply this method to determine the actual three-dimensional distribution of the air bubbles in the ice sample. In order to show the air bubbles on the ice surface conspicuously, we put carbon powder in the air bubbles that appeared as small hollows on the surface. To mask the air bubbles inside the ice, steam was sprayed on the surface. Then, the sample was photographed with an Olympus L1400 digital camera. A three-dimensional distribution of the air bubbles in the ice sample is obtained by piling up images of 0.25 mm depth interval.

3. Results and discussion

3.1. Simple image analysis of scattering images

Figure 2 shows a scattering image of an ice sample when a laser beam is irradiated at $z=1$ mm from the observation surface. Each image is composed of 720×480 pixel, which corresponds to an area of about 35×25 mm. The spatial resolution of a pixel is about 0.05 mm. The ice glitters from the air bubbles along the axis of the laser beam. We make a laser tomograph image of the ice sample mosaicking that part of each image around the center of the laser beam.

In order to evaluate how the laser tomograph image shows the actual distribution of air bubbles, we use total intensity along the axis of the laser beam, as in the following equation:

$$\text{Total intensity } (x)=\sum_{y} f\,(x,y). \tag{1}$$

Here, $f\,(x,y)$ is the intensity at a pixel (x,y) in the laser tomograph image. Directions of x and y are shown in Fig. 1. Profiles of the total intensity by the laser tomograph measurement are compared with the actual distribution of the air bubbles in

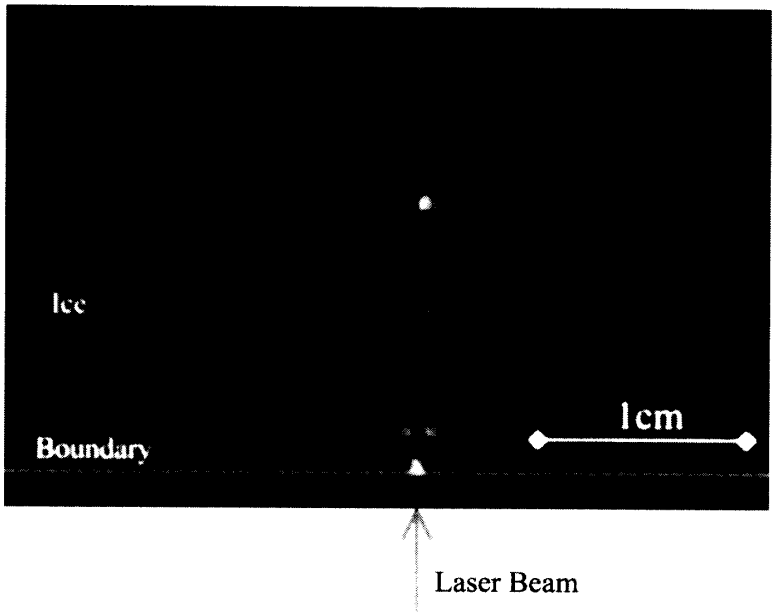

Fig. 2. A scattering image of an ice sample when a laser beam irradiated at $z=1$ mm from the observation surface.

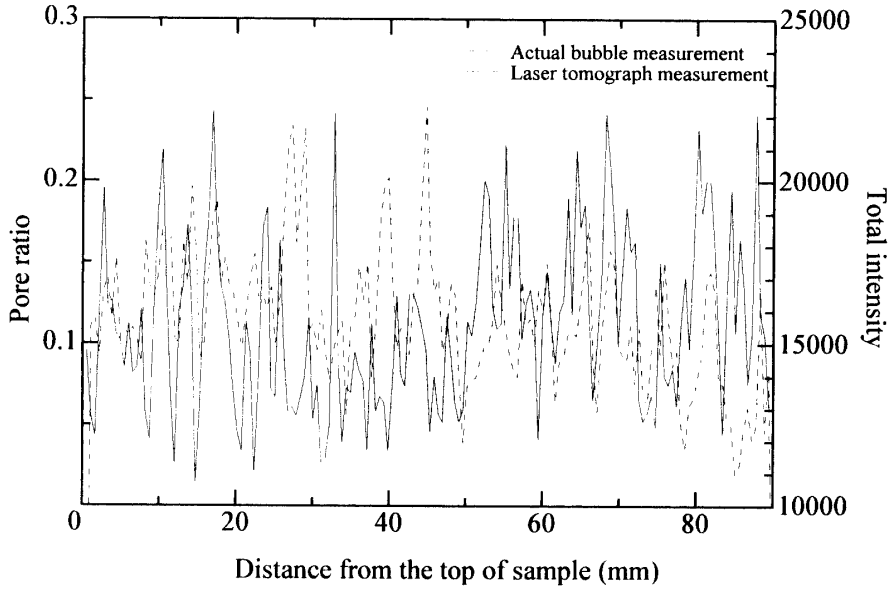

Fig. 3. Profiles of total intensity obtained by the laser tomograph measurement (solid line) and actual distribution of air bubbles (dot line).

the range of $z=0$–1.0 mm. The comparison is shown in Fig. 3.

The correlation coefficient between the two profiles is only 0.16. Possible reasons for the poor correlation are: (1) Although the intensity of a laser beam in pure ice does not decrease very much with distance, it does however decrease significantly in a "bubbly" ice sample due to scattering by the air bubbles in the ice. Therefore, the trend of scattering intensity due to air bubbles decreased with distance from the laser incident

point. In particular, air bubbles located behind somewhat larger air bubbles do not glitter. (2) Even in the absence of any air bubbles, strong scattering occurs around the incident point of the laser beam. This result indicates that actual air bubbles cannot be evaluated using the raw intensities of the scattering images. Therefore, we need to improve the image analysis algorithm. And we also need to determine effective ranges which can be analyzed for the distribution of air bubbles by the laser tomograph measurement.

3.2. *Two improvements of image analysis algorithm*

We introduce two image analysis algorithms to solve the above problems. First, we introduce a binarization process to distinguish scattering pixels at air bubbles from others for all scattering images. Figure 4 shows an example of the binarization process of a scattering image. The threshold value should be large near the incidence point of the laser beam and decrease with distance from the incidence point. But it is difficult to determine the value theoretically in bubbly ice samples. We, therefore, determine it using all of the scattering images obtained from the 9 cm long ice sample. The intensity distribution of the two-dimensional average of all of the scattering images is shown in Fig. 4a. Before the two-dimensional average is calculated, an average and its standard deviation, σ, of noise intensities are obtained from blank images, and the average and 3σ are subtracted from the original scattering images for all pixels in order to eliminate the noise.

Figure 4b shows the averaged intensity profile along the axis of the laser beam. Intensity shown in Fig. 4a and 4b indicates a large value at the laser incident point, with a remarkably rapid decrease in intensity with distance from the incident point. We use the two-dimensional average as a distribution of threshold values of the binarization for this sample. An example a scattering image derived by subtracting the average and 3σ of noise intensities from the original image is shown in Fig. 4c. Strong and weak scattering occur in the sample, although the weak scattering cannot be seen in Fig. 4c due to printing quality. Figure 4d shows intensity profiles of the image (Fig. 4c) and the threshold value distribution along the axis of the laser beam. In the binarization process, a pixel is judged as an air bubble when the scattering intensity is larger than the threshold value of the pixel. Figure 4e is a binarization image of Fig. 4c using the distribution of threshold values of Fig. 4a. Figure 4f is the result of the binarization along the laser beam axis.

Although scattering can be seen even away from the laser incident point in Fig. 2, indicating the presence of air bubbles along the laser beam axis, it is not seen in Fig. 4c. This demonstrates that further improvement of the image analysis is required to detect the air bubbles. We also consider the possibility of scattering not only at the laser axis but also around it. The difference of two serial image distances is 0.17 mm in the x direction. The reliability of detection of air bubbles is improved when binarized intensities at each pixel on many serial images around the laser beam axis are stacked to the laser tomograph image after determining a stacking position. We use part of an image with 100 pixel in width, about 5 mm, around the laser beam axis where scattering strongly occurs (see Fig. 2 or 4c). Calculating from the speed of the moving stage and resolution of the image, intensity of a pixel of the laser tomograph image is obtained by

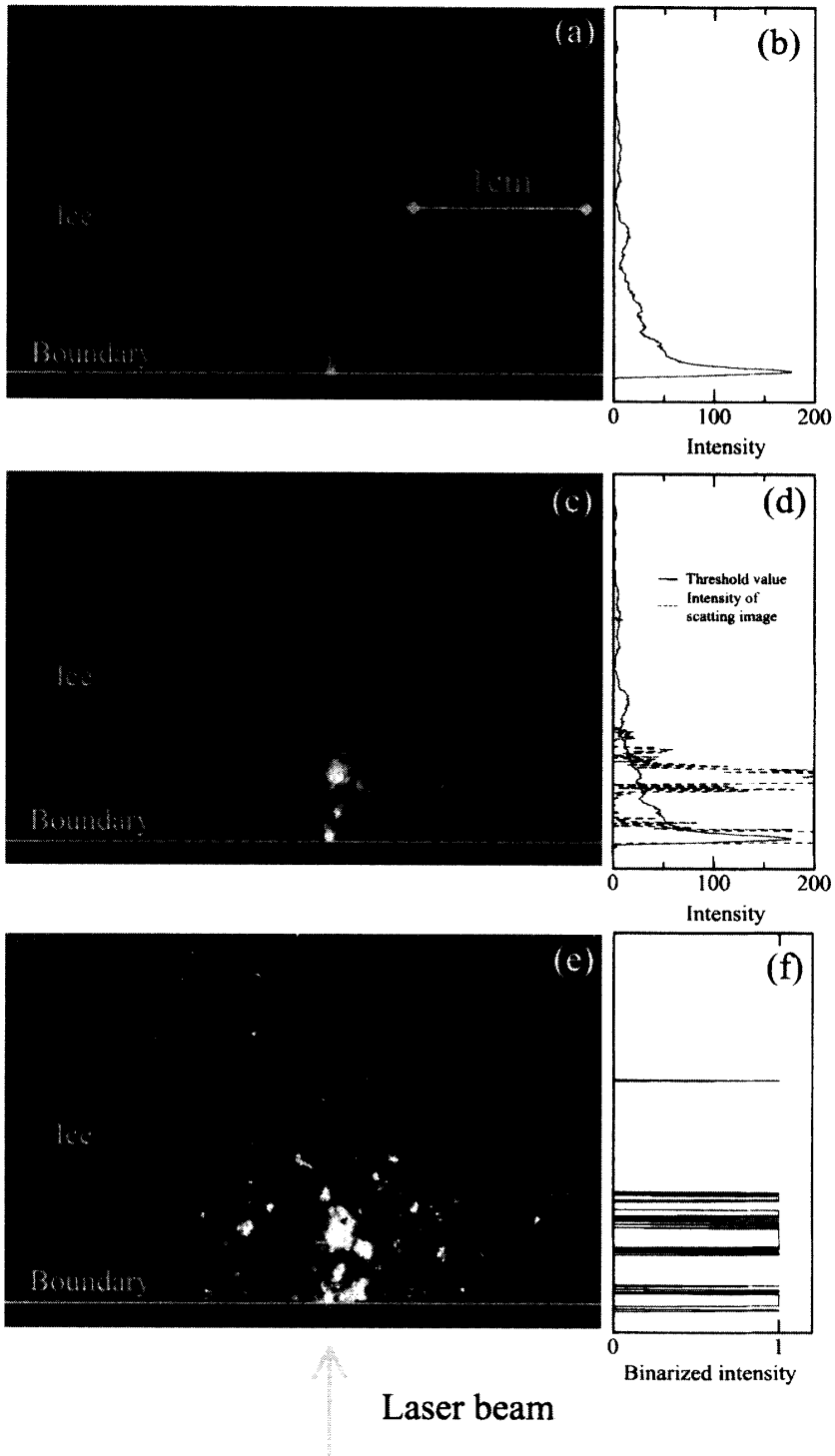

Fig. 4. Binarization process of a scattering image. (a) Intensity of threshold distribution which is determined by averaging all the scattering images after eliminating noise. (b) Intensity profile on the axis of the laser beam of the threshold value distribution. (c) An example a scattering image after eliminating noise. (d) Intensity profiles on the axis of laser beam of the threshold value distribution (solid line) and the scattering image (dot line). (e) A binarization image of the scattering image (Fig. 4c) using the threshold distribution (Fig. 4a). (f) A binarization result on the laser beam axis.

integrating intensities at the pixel on 27 serial binarization images.

A flow chart of the image analysis technique which incorporates the two improvements of binarization process of scattering images and stacking of many serial images is shown in Fig. 5. An improved laser tomograph image of the ice sample using abovementioned algorithms and actual air distribution in the range of $z=0$–1.0 mm is shown in Fig. 6. We judge a pixel to be an air bubble when scattering at the point occurs in more than 9 out of the 27 integrated images. After a series of trials, we believe this criterion for the presence of an air bubble in ice to be quite suitable.

3.3. *Effective area and depth ranges of ice sample for analysis*

Although the image analysis method is improved, we still have too much enhancement of the laser beam scattering near the incident point and not enough enhancement away from the incident point. Thus we need to evaluate the effective area in the direction of the laser beam axis (direction y in Fig. 1). We divide direction y of the improved image into 11 areas and calculate the coincidence ratio of the scattered parts in each area in Fig. 6a with that in Fig. 6b, which shows the actual air bubble distribution in the range of $z=0$–1.0 mm. The width of the area is 40 pixel, about 2 mm.

Figure 7 shows the coincidence, overestimate and undetected ratios of the scattered part and actual air bubble in the range $z=0$–1.0 mm. Overestimate means that a laser tomograph measurement indicates the presence of an air bubble when there is none, while undetected means that it indicates no air bubble when there is one. In area 1, the

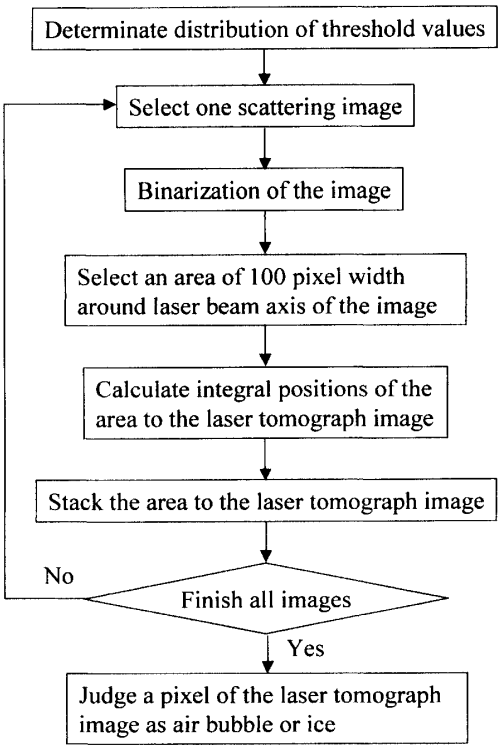

Fig. 5. Flow chart of the improved image analysis procedure for the laser tomograph measurement.

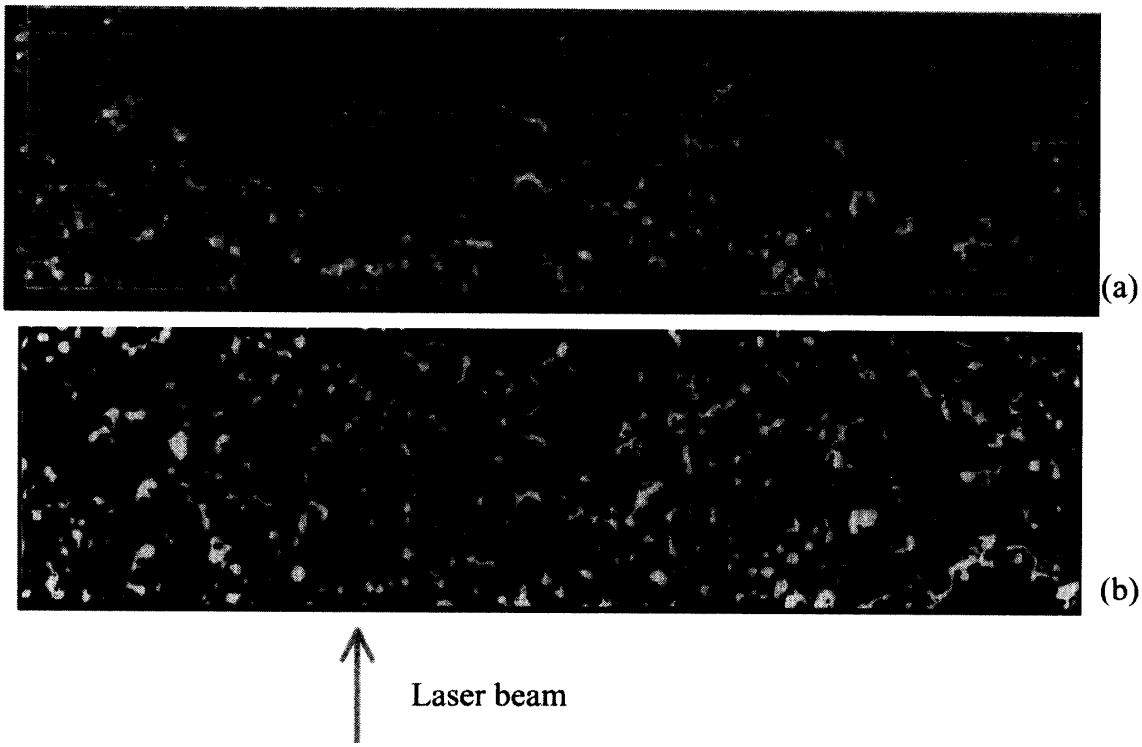

Fig. 6. (a) The improved image obtained by laser tomograph measurement. Area numbers correspond to those in Fig. 7. (b) Actual air bubble distribution in the range of $z=0$–1.0 mm.

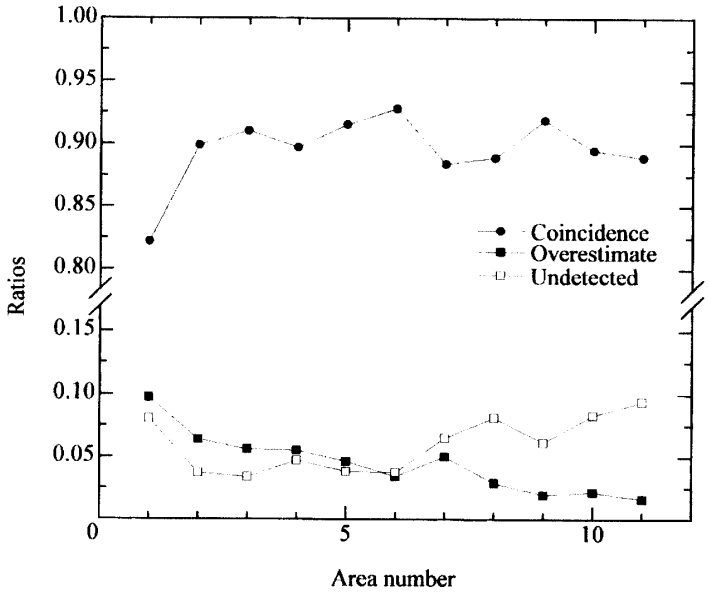

Fig. 7. Evaluation of the effective area in the direction of laser beam axis, y, of laser tomograph measurement. Divisions of area is shown in Fig. 6a.

coincidence ratio is low and the overestimate ratio is high because strong scattering occurs near the laser beam incident point. In the areas between 2 and 6 the coincidence ratios are higher than 0.9. And in the areas beyond 7, the coincidence ratios decrease with the area number because of an increase in the undetected ratio. For a stratigraphic structure measurement, a continuous high coincidence area is required. Therefore, areas between 2 and 6, which is 2 mm to 12 mm from the laser beam incident point, is a useful measurement range.

We then consider an effective depth range (z direction in Fig. 1) when the laser beam is irradiated at $z=1$ mm from the observation surface. We compare the result of the laser tomograph measurement with the actual distribution of the air bubbles in each of the 0.25 mm deep layers. Figure 8 shows the coincidence ratio between the measurement and the actual air bubble distribution in each layer. The ratio is high in the range $z=0$–1.0 mm. Below $z=1$ mm, the coincidence ratio shows low constant values. This result suggests that the laser tomograph analysis could detect most air bubbles located above the laser beam axis. We, therefore, use the actual air bubble distribution at this range $z=0$–1.0 mm to compare with the measurements results.

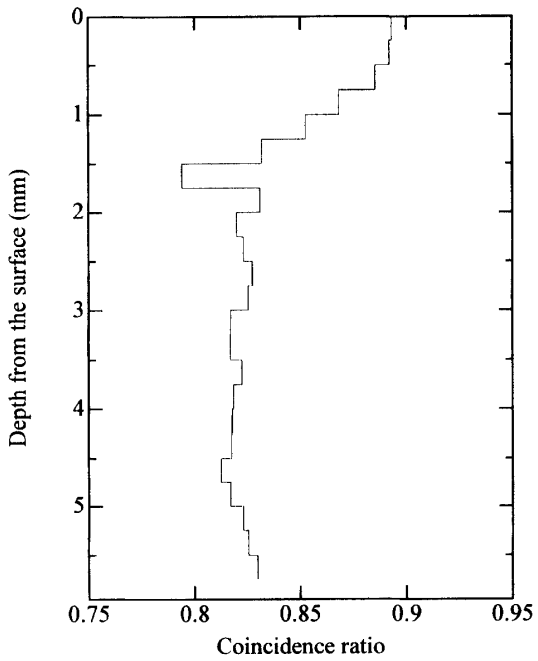

Fig. 8. Determination of effective depth range in the z direction when laser beam irradiates at $z=1$ mm from the observation surface.

3.4. Comparison of the laser tomograph measurement and actual air bubble distribution

Using the above optimum conditions and analytical algorithms, the distribution of the air bubbles determined by the laser tomograph measurement is compared with the actual distribution in the range of $z=0$–1.0 mm, as shown in Fig. 9. Two-dimensional comparison of the laser tomograph and conventional methods shows good agreement, with a coincidence ratio of over 0.9 (Fig. 9a). The profiles of the pore ratios obtained

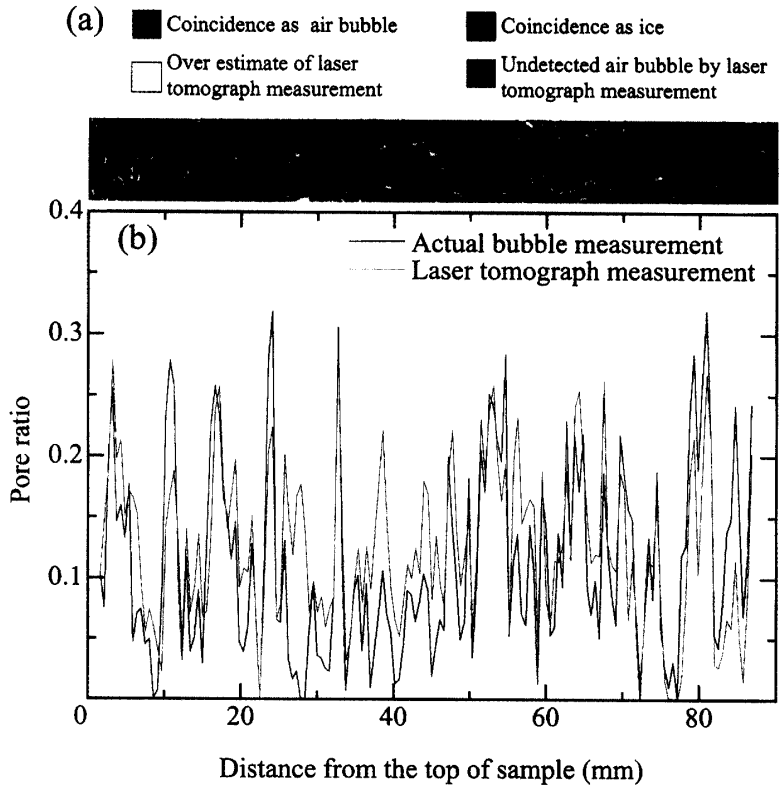

Fig. 9. Comparison of distribution of air bubbles obtained by laser tomograph measurement using optimum conditions and algorithms with actual air bubble distribution in the range z=0-1.0 mm. (a) Two-dimensional comparison. (b) Comparison of air bubble profiles.

by both methods are shown in Fig. 9b. They indicate a good relationship, with a coefficient of 0.80, and fluctuations of the profiles harmonize well with each other. Averages of two pore ratios are almost the same and the dispersion of residual error is 3.25×10^{-3}. Some pixels are still overestimated or undetected slightly (Fig. 9a), resulting in the difference of the pore ratios obtained by both methods (Fig. 9b).

4. Conclusions

We have developed a laser tomograph technique and an image analysis algorithm in order to analyze the detailed distribution of air bubbles. The measurement can be carried out very quickly (about $5\,\mathrm{mm\,s^{-1}}$). This method makes ice core stratigraphy measurement objective and high-resolution analysis possible. We introduce two improvements of the binarization process of the scattering images and stacking of many serial images for the image analysis. The effective area and depth ranges of ice sample for analysis are investigated for this measurement. After the improvements and the evaluations, the profile and distribution of air bubbles can be measured well. But further improvements can still be made on image analysis speed and limited area of reliable detection of air bubbles. We will also need to modify some parameters of the image analysis in order to improve the quality of the laser tomograph measurement. We may need to change the detecting devices, especially the capturing board, to improve

the quality of laser tomograph measurement.

Acknowledgments

The authors thank Prof. O. Watanabe of the National Institute of Polar Research for his support of this study. We also thank Prof. H. Shoji of Kitami Institute of Technology and Dr. N. Azuma of Nagaoka University of Technology for their helpful comments during this work. We also give special thanks to Dr. S. Morimoto of the National Institute of Polar Research for his considerable assistance with the image analysis programming.

References

Azuma, N., Goto-Azuma, K. and Nakawo, M. (1994): Photometric analysis of a 100 m ice core from Asuka Camp, East Antarctica: Preliminary results. Bull. Glacier Res., **12**, 69–75.

Fujii, M. (1997): Analysis of Dome F deep ice cores using laser tomography. Master's thesis, Hokkaido University (in Japanese).

Gerland, S., Oerter, H., Kipfstuhl, J., Wilhelms, F., Miller, H. and Miners, W.D. (1999): Density log of a 181 m long ice core from Berkner Island, Antarctica. Ann. Glaciol., **29**, 215–219.

Hori, A., Tayuki, K., Narita, H., Hondoh, T., Fujita, S., Kameda, T., Shoji, H., Azuma, N., Kamiyama, K., Fujii, Y., Motoyama, H. and Watanabe, O. (1999): A detailed density profile of the Dome Fuji (Antarctica) shallow ice core by X-ray transmission method. Ann. Glaciol., **29**, 211–214.

Kawamura, T. (1990): Nondestructive, three-dimensional density measurement of ice core samples. J. Geophys. Res., **95**, 12407–12414.

Kimura, T. (1983): Preliminary experiments of snow-density meter by gamma-ray scattering. Seppyo (J. Jpn. Soc. Snow Ice), **45**, 119–124 (in Japanese with English abstract).

Nishida, K. and Narita, H. (1996): Three-dimensional observations of ice crystal characteristics in polar ice sheets. J. Geophys. Res., **101**, 21311–21317.

Ram, M., Illing, M., Weber, P., Koenig, G. and Kaplan, M. (1995): Polar ice stratigraphy from laser-light scattering: Scattering from ice. Geophys. Res. Lett., **22**, 3525–3527.

(Received April 18, 2000; Revised manuscript accepted September 1, 2000)